Geometrical Nonlinearities on the Bearing Capacity in Clay
A Validation Data Set for Numerical Tools

Zwanenburg, Cor; Wittekoek, Britt; Alderlieste, Etienne; Martinelli, Mario

DOI
10.1061/JGGEFK.GTENG-12104

Publication date
2024

Document Version
Final published version

Published in
Journal of Geotechnical and Geoenvironmental Engineering

Citation (APA)
Zwanenburg, C., Wittekoek, B., Alderlieste, E., & Martinelli, M. (2024). Geometrical Nonlinearities on the Bearing Capacity in Clay: A Validation Data Set for Numerical Tools. *Journal of Geotechnical and Geoenvironmental Engineering*, *150*(10), Article 04024084. https://doi.org/10.1061/JGGEFK.GTENG-12104

Geometrical Nonlinearities on the Bearing Capacity in Clay: A Validation Data Set for Numerical Tools

Cor Zwanenburg, Ph.D.[1]; Britt Wittekoek[2]; Etienne Alderlieste[3]; and Mario Martinelli, Ph.D.[4]

Abstract: A series of plate loading tests on clay has been conducted in the centrifuge. The aim of the tests is to create a data set, which is freely downloadable, to validate numerical tools that account for geometrical nonlinearities. The tests include two sources of geometrical non-linearities. The first source is the reducing clay layer thickness below the plate, which causes an increase in resistance. The second source is the backflow of the clay around the tip of the plate. The backflow has a reducing effect on the plate resistance. This paper outlines four tests: two involving a wide plate and two with a small plate. Each plate geometry is investigated under both smooth and rough side model boundaries. An material point method (MPM) schematization is used for numerical analysis. The schematization and parameter selection are initially validated by comparing the MPM results against CPTu data in each test. The numerical analysis examines the impact of a finite layer thickness by analyzing various layer thicknesses. Furthermore, the analysis shows the influence of the backflow on the plate resistance by analyzing different ratios of shaft to plate width. In this study, the pore pressures below the plate and vertical and horizontal displacement fields are considered in addition to the load displacement curves. The MPM simulations are in good agreement with the centrifuge data. **DOI: 10.1061/JGGEFK.GTENG-12104.**

Author keywords: Soft soils; Large strain; Centrifuge testing; Numerical analysis; Material point method (MPM).

Introduction

In the development of reliable software tools for practical engineering applications, validation and verification play an important role. Analytical solutions serve as powerful tools for this purpose, offering precise insights and predictions under specific, simplified conditions. In the field of soil mechanics, these analytical solutions often rely on assumptions that the soil behaves rigidly, exhibiting a perfectly plastic response. Moreover, these solutions typically assume a fixed geometrical configuration. For instance, distinct schemes are employed to describe shallow and deep bearing capacity, with and without gap closure.

The advantage of analytical solutions lies in their ability to provide direct outcomes, making them accessible and comprehensible. However, these solutions encounter limitations when dealing with challenging configurations within deformable soils in large-displacement problems, such as bearing capacity problems, where evolving geometries are induced.

To overcome these limitations and obtain a comprehensive understanding of soil behavior in such configurations, the development of experimental tests becomes imperative. These experiments provide essential insights into the actual behavior of soils under conditions that deviate from the simplified assumptions of analytical solutions. By conducting experiments that simulate real-world scenarios more accurately, engineers and researchers can gather empirical data crucial for validating theories, refining models, and developing more accurate predictions for complex soil behaviors.

This paper presents a series of centrifuge tests conducted to validate numerical tools. The test series comprises plate loading tests, wherein the plate penetrates the soil for a depth exceeding 95% of the original layer thickness. This paper details the experimental setup and the obtained results. The test data is publicly available (Zwanenburg et al. 2023b).

This paper follows the original test numbering system, where Test 1 involves the wide plate and smooth boundaries, Test 3 encompasses the small plate and smooth boundaries, Test 6 includes the small plate and rough boundaries, and Test 8 comprises the wide plate and rough boundaries. The test numbers in between pertain to tests on a peat layer, detailed in Zwanenburg et al. (2023a).

Furthermore, the paper includes a section with the results of a numerical model (Martinelli and Galavi 2022) based on the material point method (MPM). This model effectively depicts soil-structure interaction in scenarios involving large-displacements. It accurately simulates data from cone penetration tests with pore pressure measurement (CPTu) and plate penetration tests, accounting for the influence of backflow (gap-closure) and variable soil thickness on the soil bearing capacity.

This paper is composed of a description of the relevant phenomena in the "Theoretical Background" section, followed by a description of the test setup in the section "Setup of the Centrifuge Tests." The "Tested Material" section discusses the characteristics of the tested material. The actual subsoil strength obtained during flight

[1]Deltares, P.O. Box 177, 2600 MH, Delft, Netherlands; Faculty of Civil Engineering & Geosciences, Dept. of Geo-Engineering, Delft Univ. of Technology, Delft, Netherlands (corresponding author). ORCID: https://orcid.org/0000-0002-8493-6943. Email: cor.zwanenburg@deltares.nl

[2]Deltares, P.O. Box 177, 2600 MH, Delft, Netherlands. Email: britt.wittekoek@deltares.nl

[3]Deltares, P.O. Box 177, 2600 MH, Delft, Netherlands; presently, Equinor ASA, P.O. Box 3, Fornebu 1330, Norway. Email: eald@equinor.com

[4]Deltares, P.O. Box 177, 2600 MH, Delft, Netherlands; Adjunct Research Professor, Dept. Civil and Environmental Engineering, Carleton Univ., Ottawa, ON, Canada. Email: mario.martinelli@deltares.nl

Note. This manuscript was submitted on July 12, 2023; approved on February 26, 2024; published online on July 18, 2024. Discussion period open until December 18, 2024; separate discussions must be submitted for individual papers. This paper is part of the ***Journal of Geotechnical and Geoenvironmental Engineering***, © ASCE, ISSN 1090-0241.

is explained in the section "Strength Profile, Comparison CPTu, and Laboratory Test Data," followed by a description of the test results in the "Centrifuge Test Results," the numerical results in the "MPM Analysis" section and the "Discussion" section. The paper finalizes by conclusions discussed in the final section.

Theoretical Background

The analysis of the bearing capacity of a plate pushed into the soil and its application in different engineering fields has a long history. Among others, Prandtl (1920), Buisman (1940), Meyerhof (1951, 1963), Brinch Hansen (1970), Das (2007), and Van Baars (2018) have studied the bearing capacity of shallow foundations. Other applications can be found in spudcan design in offshore engineering, e.g., Hossain et al. (2004, 2006) and Ullah and Hu (2017).

Literature shows that a succession of different failure mechanisms will develop during penetration. At shallow depth the plate might act as a shallow foundation resulting in a shear failure mechanism, Fig. 1(a). For soft soils, punching shear might develop for undrained loading conditions, Fig. 1(b). Since the plate is wider than the shaft, cavities will form at both sides of the shaft. At some depth backflow of the clay around the tip of the plate into the cavity will dominate the failure pattern, Fig. 1(c).

For the individual mechanisms, analytical solutions are available. The corresponding undrained bearing capacity, q_u is given by Das (2007):

$$q_u = N_c s_u + \sigma_v, \qquad N_c = 2 + \pi \quad \text{for} \quad \frac{B}{2H} < \frac{\sqrt{2}}{2}$$
$$q_u = N_c^* s_u + \sigma_v, \qquad N_c^* = 2 + \pi + \frac{B}{2H} - \frac{\sqrt{2}}{2} \quad \text{for} \quad \frac{B}{2H} \geq \frac{\sqrt{2}}{2} \tag{1}$$

In which N_c represents the bearing capacity factor, s_u the undrained shear strength, σ_v represents the overburden pressure. Plate width, B, and layer thickness, H, are defined in Fig. 1.

Resistance due to backflow of the clay follows from (Hossain et al. 2006)

$$q_u = N_{cd} s_u + \frac{\gamma' V}{A} \tag{2}$$

In which N_{cd} = bearing capacity factor for the backflow mechanism, γ' = effective weight of the soil, V = volume of the embedded plate, and A = superficial area of the plate.

For large penetration depth, and consequently small H, the resistance is expected to increase due to extra resistance at the bottom of the layer. This is accounted for in Eq. (1) by the term $B/2H - \sqrt{2}/2$. In the following, this is referred to as the finite layer effect. Eq. (2) does not account for the finite layer effect.

Setup of Centrifuge Tests

The centrifuge tests are conducted in the Deltares Geo-centrifuge (Zwaan et al. 2020). A 100 mm thick Kaolin clay layer was placed in a strong box, with inner dimensions $200 \times 450 \times 870$ mm (width × height × length). Details of the clay are given in the section "Tested Material." A sketch of the front view of the set-up is given by Fig. 2. The model included an aluminum bottom plate, which contained a drainage system to allow for in-flight consolidation, see Fig. 3. A loading plate was placed at the center of the model. The plate length, perpendicular to the front and back wall was 195 mm, leaving some space between the plate and the walls. In this way, friction between the plate and walls was avoided. Tests were conducted with a 20 mm and 100 mm wide plate. It should be noted that B/H = 1 for the 100 mm wide plate at the start of the test. The shaft width, d in Fig. 1(c), was 10 mm for the small plate and 30 mm for the wide plate. Both smooth and rough boundary conditions were applied at the bottom of the plate, as well as below the clay layer on the drainage plate. Smooth conditions were represented by polished steel, while rough conditions were created by placing skateboard grip tape on the bottom plate and loading plate.

The instrumentation included 16 total pressure cells, mounted in the bottom plate and walls of the strongbox. In total 3 or 4 direct current displacement transducers, DCDTs, were placed at the right side of the plate to measure heave next to the plate, see Fig. 2. Nine pore pressure sensors were placed in the bottom plate and side wall of the strongbox and 2 pore pressure sensors in the bottom of each of the loading plates. Two L-VIT 2500 Color cameras, 7,920 × 6,004 pixels, were placed in front of the model. Soil deformations were obtained by particle image velocimetry, PIV, analysis using the GeoPIV-RG software (Stanier et al. 2015). The displacement of

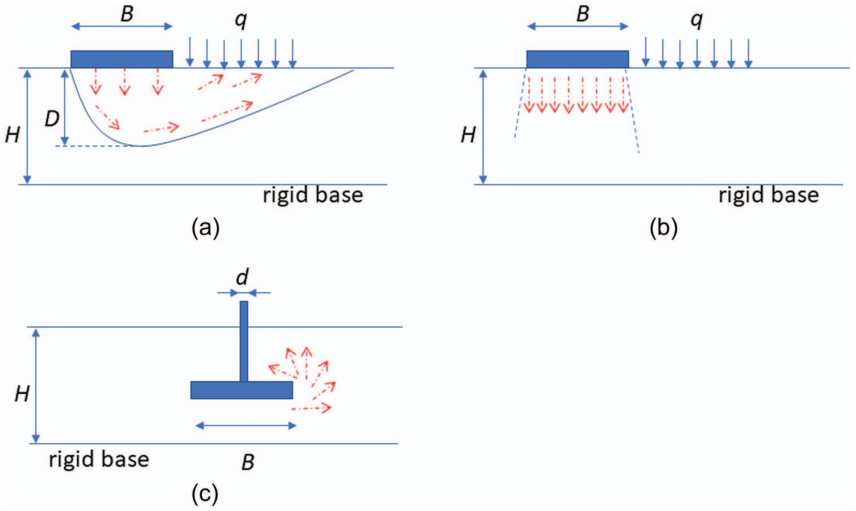

Fig. 1. (Color) Failure mechanisms: (a) slip plane failure; (b) punching shear; and (c) backflow, blue solid arrows indicate surface loads, red broken arrows sketch the displacement field.

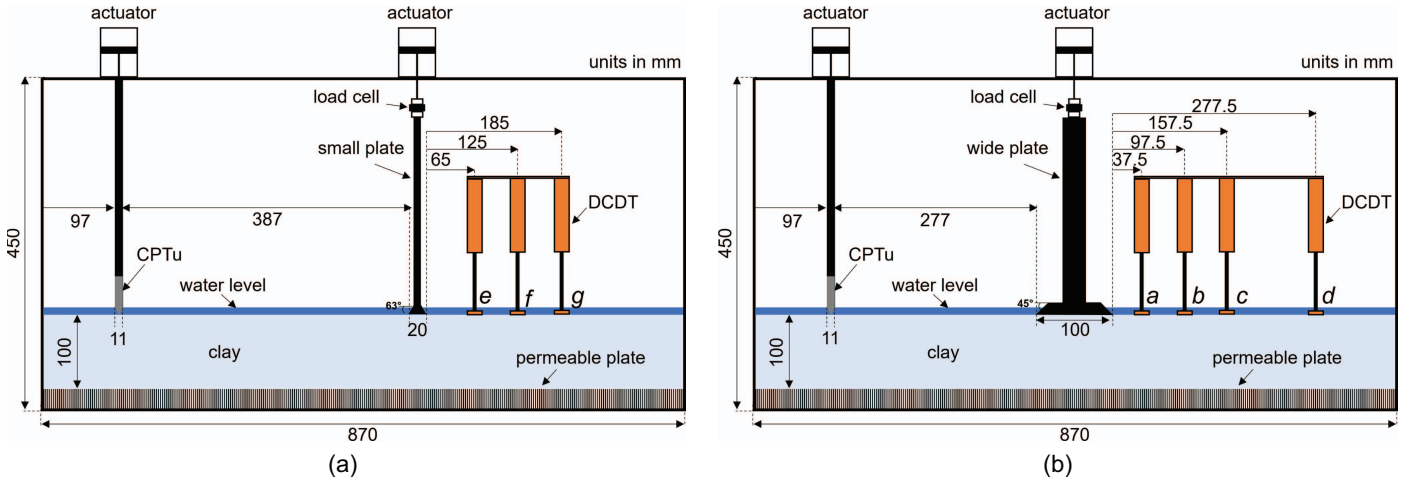

Fig. 2. (Color) Sketch of the test set-up in front view (a) for the wide loading plate; and (b) for the small loading plate.

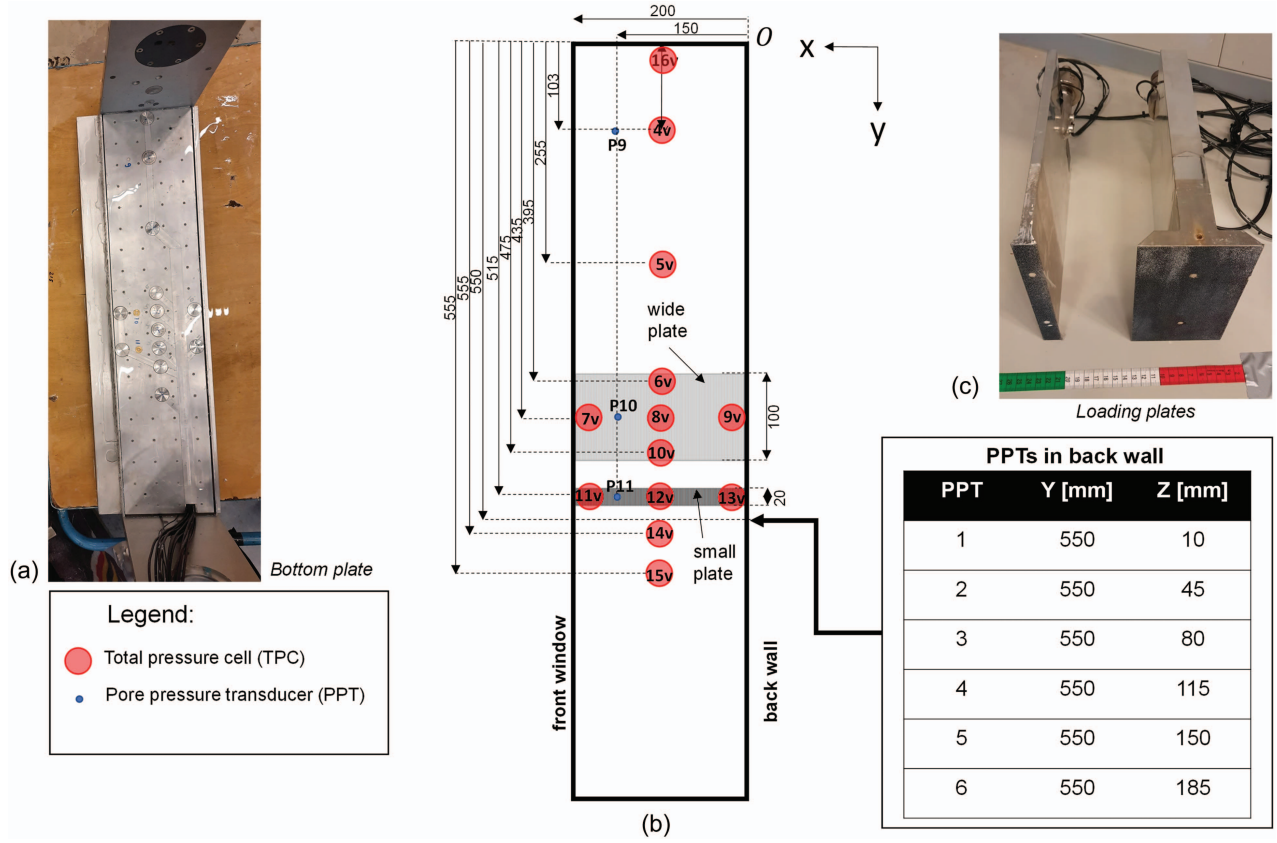

Fig. 3. (Color) Components of the test set up, measures in (mm): (a) drainage plate; (b) instrumentation in top view; and (c) loading plates.

the plate was measured and controlled by a hydraulic actuator, with a maximum stroke of 250 mm. The force was measured by a load cell, type U9C, with a measurement range of 0–50 kN. Drainage of the clay layer was allowed through top and bottom. To prevent drying of the clay and to avoid uncertainty on the position of the phreatic level, a water layer was present on top of the model. The free water on top of the model also prevented desaturation of the pore pressure sensors mounted at the bottom of the loading plates. The outflow of the bottom plate and water layer at the top were connected to assure the same hydraulic head at top and bottom of the clay.

The tests contained four phases. First, the centrifuge was spun to 100 g at 10 g/min. Second, the clay layer consolidated until the excess pore pressure was less than 1 kN/m^2. In this context, excess pore pressure is defined as the pore pressure exceeding the hydrostatic pressure. Third, the plate was pushed into the soil with a velocity of 5 mm/min. During penetration the camera frequency was 1 Hz, resulting in 1 photo per 0.083 mm displacement for each camera. Penetration was stopped at 4 mm above the bottom of the clay layer to prevent damage of the equipment. Fourth, a CPTu measurement was conducted to evaluate the clay strength. For this purpose, a mini-CPTu was used. The dimensions are presented in

J. Geotech. Geoenviron. Eng., 2024, 150(10): 04024084

Table 1. Dimensions of the CPTu cone

Parameter	Symbol	Unit	Value
Cone diameter	D_{one}	mm	11.3
Apex angle	θ	degrees	60
Tip height	h_{tip}	mm	9.8
Cone net area ratio	a	—	0.54
Length sleeve	h_{sleeve}	mm	42.5
Diameter sleeve	D_{sleeve}	mm	11.35

Table 2. Test overview, thickness clay, and water layer at start of penetration, phase 3

Test	Plate width (mm)	Boundary conditions	h_{clay}[a] (mm)	h_{water}[b] (mm)
1	100	Smooth	96.5	52.0
3	20	Smooth	95.0	67.2
6	20	Rough	94.1	39.2
8	100	Rough	90.8	41.8

[a]The initial clay layer thickness is 100 mm in each test.
[b]The water height on top of the clay layer.

Table 3. Properties of the clay

Parameter	Unit	Mean	CV	n
Saturated volume weight, γ_{sat}	kN/m^3	16.4	0.2	14
Water content, w	%	53.4	2.0	14
Void ratio, e	—	1.44	0.06	14
Plasticity index, PI	%	38.5	0.7	5
Liquid limit, w_L	%	66.2	1.4	5

Note: CV = coefficient of variation; and n = number of tests.

Table 4. Summary of laboratory test results

Parameter	Unit	Value
Cohesion, c'	kN/m^2	2.4[a]/0[b]
(Plain-strain) friction angle, φ'	degrees	14.3[a,c]/16[b]
Undrained shear strength ratio, S	—	0.19
Power, m[d]	—	0.8
Compression ratio, CR	—	0.19

[a]Peak strength.
[b]Strength at large strain, $\gamma = 40\%$, used as proxy for critical state strength.
[c]Numerical analysis in TX conditions uses $\varphi'_{tc} = 18.11°$.
[d]Derived from $m = (CR\text{-}RR)/CR$, with RR re-compression ratio.

Table 1. The cone was calibrated for a range of 0–150 N. The pore pressure filter was positioned above the cone, u_2 position. To avoid desaturation of the filter, the cone tip and filter were positioned in the water layer on top of the model. The distance between CPTu measurement and nearest side wall, $L_{cptu} = 97$ mm, see Fig. 2, resulting in $L_{cptu}/D_{cone} = 8.8$, with D_{cone} representing the cone diameter. Following Ullah et al. (2016) the minimum distance between the cone and model boundary, when testing uniform clay, should be $L_{cptu}/D_{cone} > 2$ for perfect smooth boundaries and $L_{cptu}/D_{cone} > 1.5$ for perfect rough boundaries. From these values, it is concluded that no interference with the model box boundaries is to be expected. The distance between the CPTu and the plate was 387 mm for the small plate and 277 mm for the wide plate. The actual clay and water layer thicknesses for the third and fourth phase were derived from the photo analysis, see Table 2.

During flight, a minor g-level increment is found along the depth of the model due to the increasing distance from the rotation point of the centrifuge. The distance from the point of rotation to the clay top is 4.795 m. The applied g-level, 100 g, is realized at the top of the clay layer before consolidation. The effect of an increasing g-level along the clay depth results in a maximum deviation of 1.8% in effective vertical stress for a 100 mm thick clay model and is neglected in the analysis.

Tested Material

The kaolin clay was mixed from a powder and water to a slurry. The slurry was consolidated in a Rowe cell under a constant overburden pressure of 40 kN/m^2. In total 2 batches have been prepared. A minor difference in water content, w was found between the batches after consolidation. In 4 measurements the water content ranged for batch 1 from 52.6% to 53.7% with an average of 53.1%. For batch 2 the water content ranged from 54.0% to 56.7% with an average of 55.5%. Material for tests 1 and 3 was taken from the first batch and material for tests 6 and 8 from the second batch. The required material for the individual tests was trimmed from the batch and the remaining batch was put in storage for the next test. The period between test 1 and 3 was 14 days, between test 6 and 8 was 7 days. During these periods the clay was wrapped in plastic foil and stored at a constant temperature of 10°C ± 0.1°C. Tables 3 and 4 summarizes the results of a series of laboratory tests, conducted on the material from the first batch, including 3 constant rate of strain tests, CRS, 2 incremental loading test, IL, 8 Direct simple shear tests, DSS and 1 consolidated undrained, CU, triaxial test. The Atterberg limits were assessed according to NNI (2018), using the fall cone for determination of the liquid limit, w_L. Following the plasticity chart (NNI 2018), the clay can be described as a highly plastic clay, ClH.

DSS testing was conducted in accordance with ASTM (2017). An overconsolidation ratio, OCR, ranging from 1.0 to 2.0 was applied. A constant height was maintained, representing undrained testing (Dyvik et al. 1987). The large strain strength, strength at a shear strain of 40%, is used as a proxy for the critical state strength (a.o. Leroueil et al. 1990). Table 4 presents the values for cohesion, c' and friction angle, φ', for peak and large strain approaches. Following the critical state theory, Wood (1990), the cohesion is set to zero for the large strain approach, while some cohesion is allowed for the peak strength approach. The values are found by curve fitting. Remarkably, the fitting results in a friction angle for large strains which is slightly larger than found for peak strengths. Due to softening the opposite trend was expected. In the numerical analysis, this issue is addressed by a validation of the parameter set by a simulation of the laboratory test results. This is further discussed in the section "Centrifuge Test Results."

The undrained shear strength parameters were evaluated by fitting the SHANSEP formula (Ladd and Foot 1974):

$$s_u = S(\mathrm{OCR})^m \sigma'_v \tag{3}$$

In which OCR and the vertical effective stress, σ'_v, follow from the test conditions. The undrained shear strength ratio, S, and power m are fitted to the laboratory data, see Table 4.

The CRS tests were conducted following ASTM (2012). Horizontal pressure gauges were added to the oedometer ring to measure the horizontal pressure (Den Haan and Kamao 2003). This allowed to assess K_0, in which $K_0 = \sigma'_h/\sigma'_v$. The tests showed that, for normally consolidated, NC, conditions, the value of K_0^{NC} was

0.72. When using the friction angle obtained from DSS testing, Jaky's relation, agrees with the K_0^{NC} from CRS testing

$$K_0^{nc} = 1 - \sin\varphi' = 1 - \sin(14.3) = 0.75 \tag{4}$$

Strength Profile, Comparison CPTu, and Laboratory Test Data

Crucial in understanding the centrifuge tests is the undrained shear strength of the clay. In-depth undrained shear strength profiles of the clay during flight are obtained from the CPTu data and compared to the laboratory test results. The interpretation of the CPTu data follows Robertson and Cabal (2015)

$$q_c = \frac{F_c}{A_c}; \qquad q_t = q_c + (1-a)u_2;$$
$$q_{net} = q_t - \sigma_v; \qquad s_u = \frac{q_{net}}{N_{kt}} \tag{5}$$

In which F_c = measured force, A_c = projected cone area, q_c = cone resistance, a = cone area ratio, here $a = 0.54$, u_2 = pore pressure just behind the tip of the cone, σ_v = overburden pressure, and N_{kt} = cone factor.

A_c increases until its maximum value is reached when the tip of the cone is fully covered in the clay. This effect was accounted for In the derivation of q_c. The tip resistance and pore pressure readings were set to zero when the tip of the cone touched the clay top. Consequently, σ_v represents the increment in overburden pressure.

Tables 3 and 4 are used to derive the in-depth strength profile based on the laboratory tests. Fig. 4 compares the in-depth profiles, for which in general a good agreement is found for tests 1, 6 and 8. The differences at the top are explained by the use of N_{kt} set to 14, which represents the condition in which the failure mechanism around the cone is fully enclosed by the clay. At a depth of 60 mm, the stress conditions, at 100 g, change from over-consolidated to normally consolidated. This results in a clear bend in the laboratory test profile, while appearing less prominently in the CPTu test results.

The divergent CPTu profile for Test 3 is remarkable and not fully understood at this moment. A possible explanation could be the storage and preparation of the clay. As explained in the section "Tested Material," the clay for Test 1 and Test 3 came from the same batch. With Test 3 being conducted two weeks after Test 1, incorrect storage procedures might have altered the clay properties. Fig. 5 shows a reasonable agreement between CPTu data and laboratory test data for Test 3 when assuming a preconsolidation stress, $\sigma'_{vc} = 62.5$ kPa instead of 40 kPa. It should be noted that tests 6 and 8 originate from the second batch and CPTu data from these tests are in good agreement to each other and to Test 1.

Centrifuge Test Results

Fig. 6 shows the load–displacement curves measured in the 4 tests. Remarkably, for the wide plates, no significant difference is found between the smooth and rough boundary conditions. For the small plate tests, the slightly larger resistance for the smooth plate can be explained by the difference in clay strength, see Figs. 4 and 5. A small difference in rough and smooth boundary conditions is also found by Hossain et al. (2006) and will be discussed further in the section "Discussion."

Until a penetration depth of about 15 mm the applied load, [kN/m^2], is equivalent for the small and wide plate. At larger depth, the resistance increases monotonically for the small plates, while the wide plates invoke less resistance. The influence of the finite layer effect is found in a clear increase in applied load and differs for the wide and small plate. For the wide plate, the finite layer effect is found at a penetration depth of approximately 70 mm, when the load–displacement curve starts to bend. For the small plate, this effect is found later, at a penetration depth of approximately 85 mm.

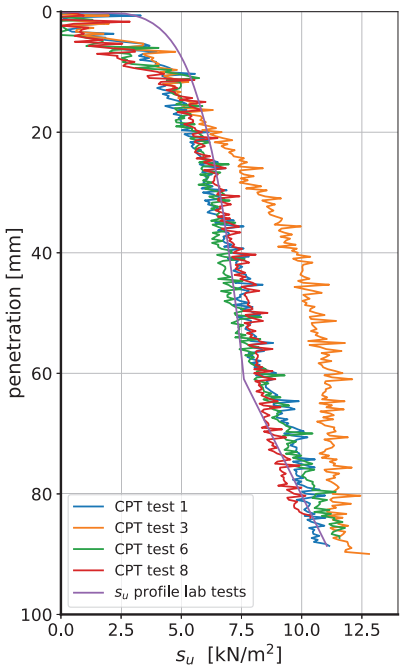

Fig. 4. (Color) In-depth profile of the undrained shear strength s_u at 100 g, derived from laboratory tests and CPTu testing.

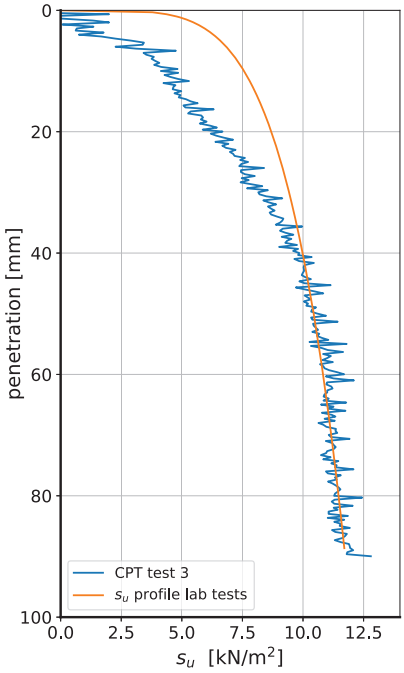

Fig. 5. (Color) Comparison s_u profile from CPTu and laboratory testing, Test 3 for $\sigma'_{vy} = 62.5$ kPa.

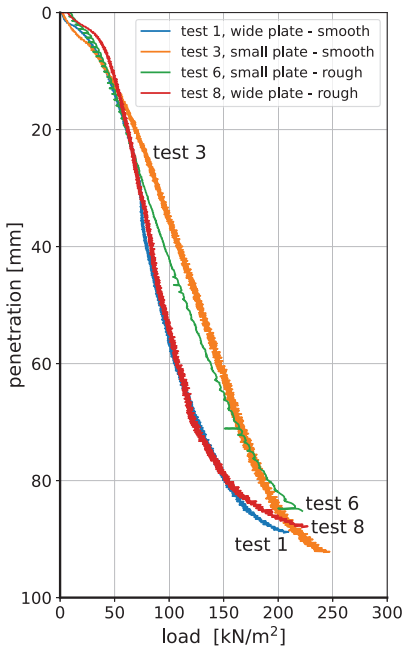

Fig. 6. (Color) Load displacement curves.

Fig. 7 shows the different displacement fields at maximum penetration for the different tests. For the wide plates, the backflow of the clay around the tip is clearly visible. Fig. 8 shows the displacement field at 4 different stages of penetration of the wide plate with smooth boundaries and Fig. 9 shows the vertical displacement of the top of the clay layer at different distances from the loading plate. For the wide plate, a succession of different failure mechanisms can be distinguished:

- At shallow depth: the displacement field, Fig. 8(b), shows the development of a sliding plane, as shown by Fig. 1(a). The top of the clay layer heaves, as found by the vertical displacement measurements in Figs. 9(a and c) until a penetration depth of 20 to 25 mm is reached. Less heave is found at larger distances from the plate. Fig. 8(b) also shows a cavity, which is created above the plate.
- At intermediate depth: when penetration exceeds 25 mm, backflow of the clay around the tip of the plate starts to fill the cavity above the plate. The heave of the top of the clay layer stops, indicated by vertical displacements measured at DCDT *b*, *c* and *d*, which remain constant at further penetration, see Figs. 9(a and c). In this stage, the backflow mechanism is not fully covered by the clay. Consequently, the top of the clay layer also flows into the cavity as shown by Fig. 8(c) and vertical displacement measurements at DCDT *a*, see Figs. 9(a and c).

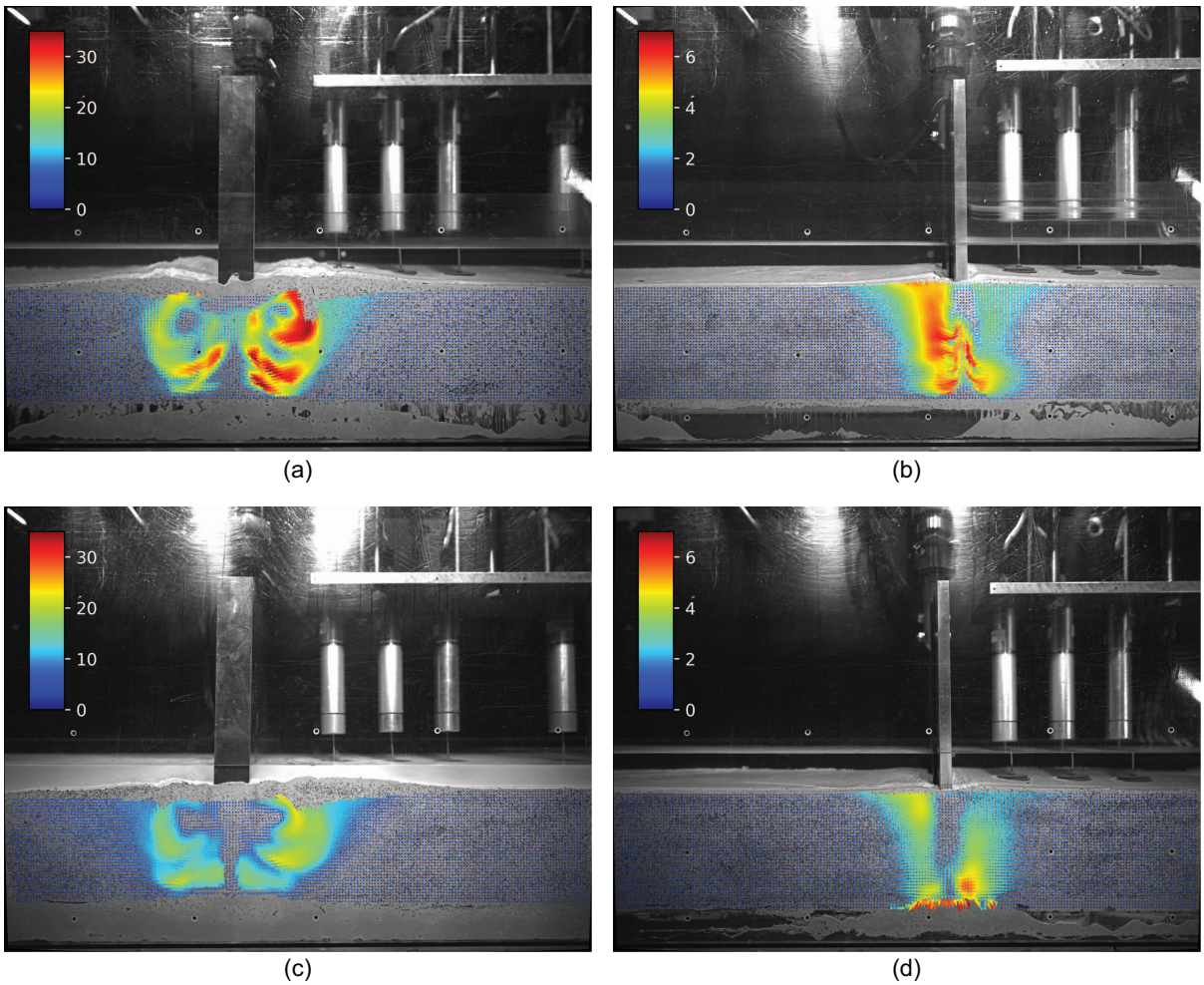

Fig. 7. (Color) Total soil displacement $\sqrt{(u_x^2 + u_y^2)}$ at final penetration depth, for (a) wide plate smooth conditions; (b) small plate, smooth conditions; (c) wide plate, rough conditions; and (d) small plate and rough conditions.

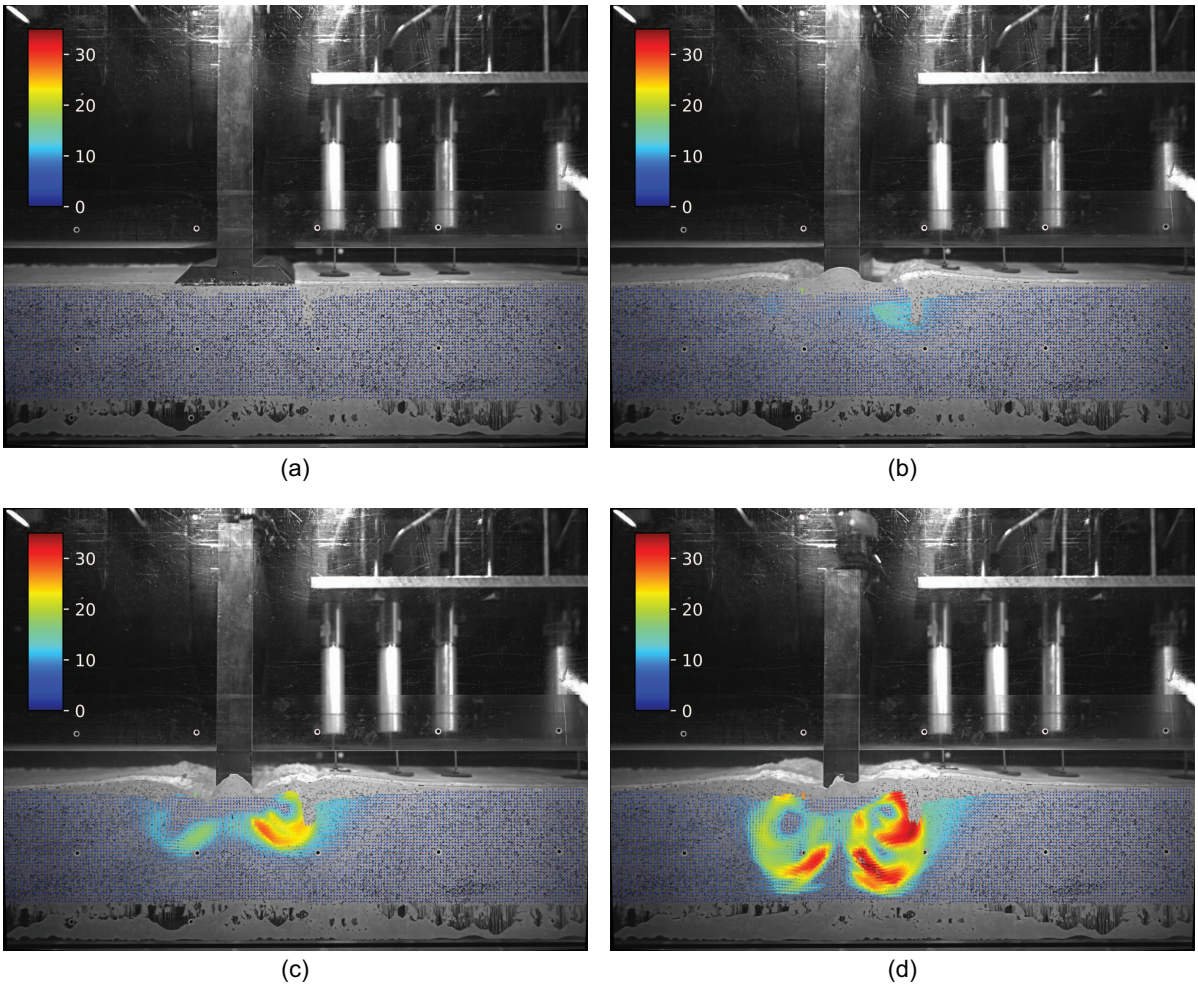

Fig. 8. (Color) Total soil displacement $\sqrt{(u_x^2 + u_y^2)}$, for wide plate and smooth boundary conditions for (a) prior to penetration; (b) at 28 mm penetration; (c) at 53 m penetration; and (d) at maximum penetration.

At increasing penetration depth, the backflow mechanism develops at a deeper level and, consequently, is increasingly more enclosed in the clay.

- At large depth: the reducing clay thickness between the plate and rigid base causes a further change in failure mechanism. The remaining clay between the plate and base is horizontally squeezed out, see Fig. 8(d), resulting in a rapid increase in applied load.

The sequence of failure mechanisms is also found in the application of Eqs. (1) and (2) to the measurement data. A good agreement is found between the test results using the small plate and Eq. (1), see Fig. 10(a). The comparison uses the laboratory test results for the undrained shear strength profile, the thin line in Fig. 4. For Test 3, small plate and smooth boundary conditions, the thin line in Fig. 5 is used. Fig. 10(b) shows that for the wide plate Eq. (1) is only in reasonable agreement with measurement data at shallow penetration depth. From a penetration depth of approximately 20 mm Eq. (1) overpredicts the resistance. This is explained by the development of the backflow mechanism. Fig. 10(c) shows the N_{cd}-values, Eq. (2), found when combining the undrained shear strength profile based on the CPTu data and the resistance measured in the centrifuge tests. To obtain this graph, the load–displacement curves, Fig. 6, have been fitted by a 5th order polynomial. The polynomial order was chosen such that for each fit the weighted least squares sum, R^2 was above 0.99. Using the fits, instead of the measurement data, results in smooth functions, except for the top, where both, the s_u profile and the stress–displacement curves reduce to 0 kN/m^2 causing strong fluctuation in N_{cd}–value for the top 5 mm of penetration. From a penetration depth of 20 mm, when Eq. (1) starts to deviate from the measurement data, a N_{cd}–value of around 10 is found for smooth conditions and 11 for rough conditions. For further increasing penetration, N_{cd} slightly increases to 12 for rough conditions and 13 for smooth conditions at a penetration depth of 70 mm. This is explained by the backflow mechanism which is more enclosed by surrounding soil at lower depth. At a penetration of approximately 70 mm, the N_{cd}–value increases further, which is explained by the finite layer effect. Hossain et al. (2006) give $N_{cd} = 10$ to 11 for circular shaped spud cans. This is in the same range but differences in shape and stress state prevent a direct comparison.

It is remarkable that Eq. (1) fits well to the small plates, although, penetration of the small plate does result in a cavity above the plate, next to the shaft. The dimensions of the plates and shafts, given in the section "Setup of Centrifuge Tests," result in a maximum of 5 mm opening for the small plate, while a 35 mm opening is found for the wide plate. Apparently, the opening width of 5 mm for the small plate is too small to have a significant influence.

The pore pressure response directly below the plate is measured by two sensors, one at the front and one at the back, mounted in the

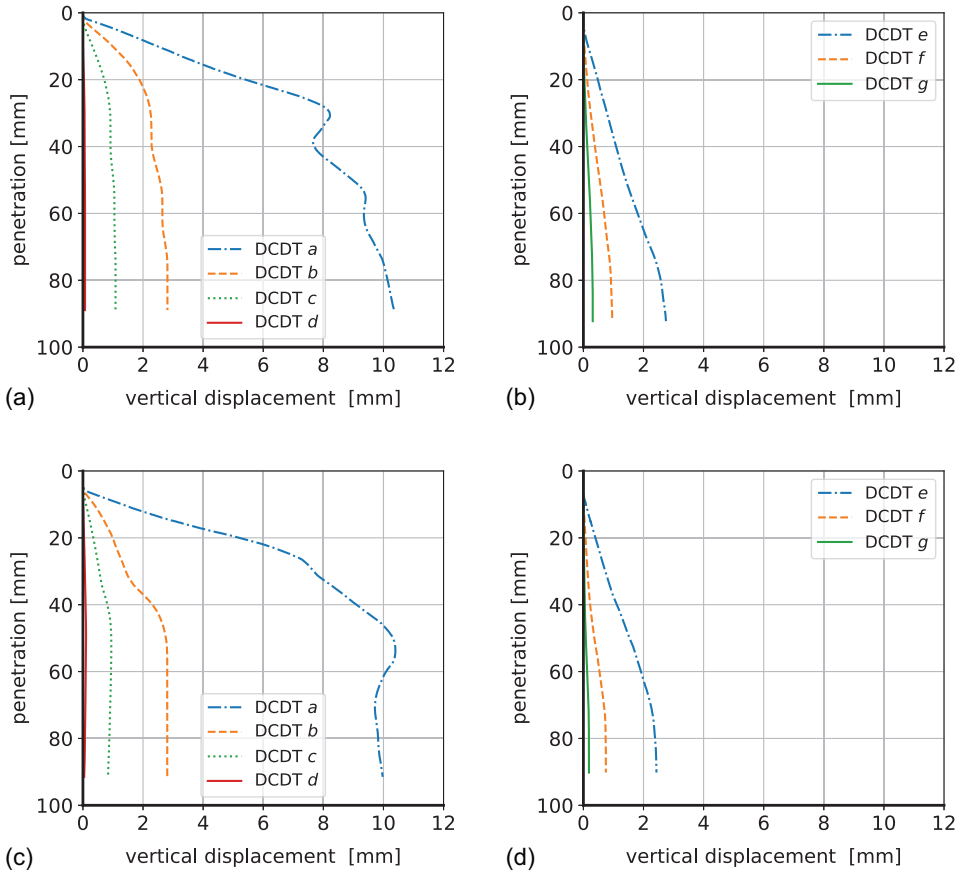

Fig. 9. (Color) Vertical displacement measured by DCDTs, for positions DCDTs see Fig. 2: (a) wide plate smooth boundary conditions; (b) small plate smooth boundary conditions; (c) wide plate rough boundary conditions; and (d) small plate rough boundary conditions.

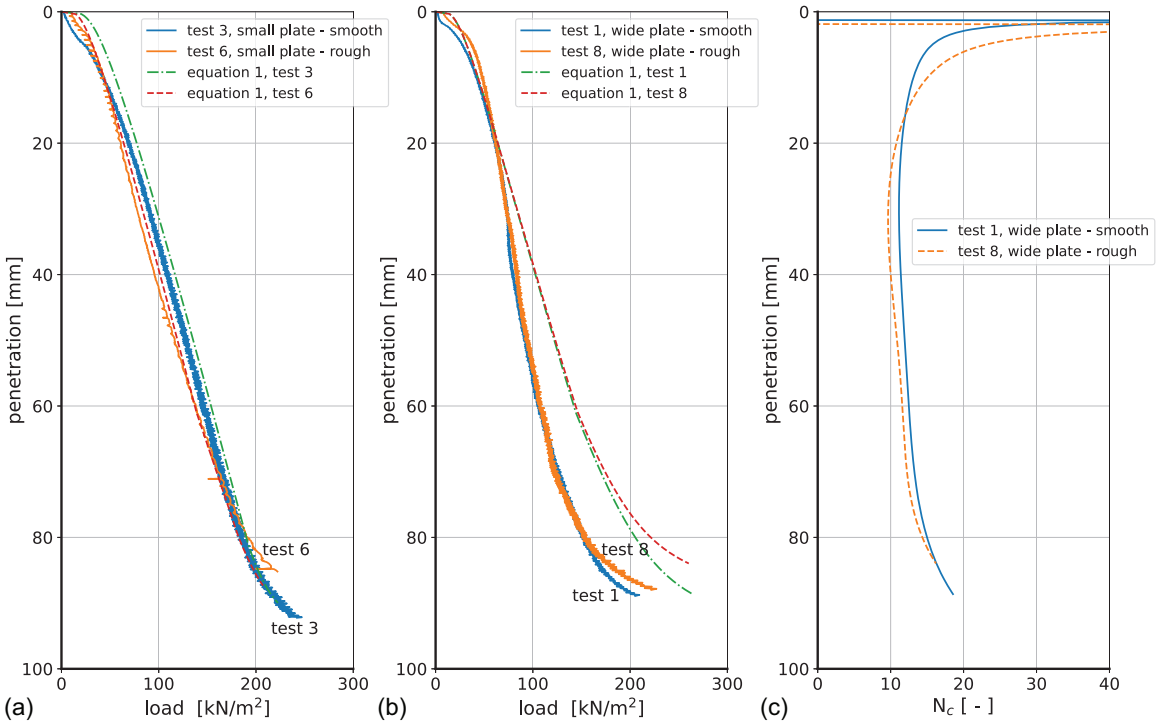

Fig. 10. (Color) Comparison measurement data to analytical solutions: (a) comparison small plate results to Eq. (1); (b) comparison wide plate results to Eq. (1); and (c) N_{cd} values, see Eq. (2) for wide plate test results.

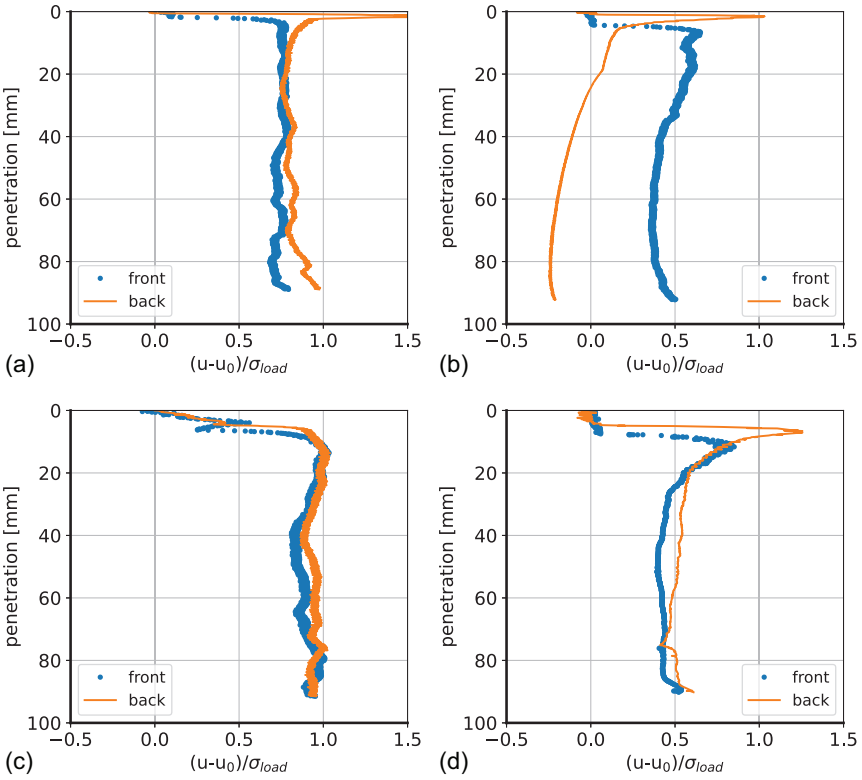

Fig. 11. (Color) Pore pressure measurements directly below the plate: (a) wide plate smooth boundary conditions; (b) small plate smooth boundary conditions; (c) wide plate rough boundary conditions; and (d) small plate rough boundary conditions.

plate bottom, see Fig. 3. Fig. 11 shows the ratio of excess pore water pressure and applied load, $(u\text{-}u_0)/\sigma_{\text{load}}$. The small and wide loading plate show a clear difference which can be explained by the dimensions of the plate. De Josselin De Jong (1963) shows that the undrained pore pressure response to loading, Δu equals the isotropic total stress increment, Δp. For one-dimensional conditions, only strain increments in vertical direction and horizontal strains prohibited, Δp equals the applied load, σ_{load} and consequently $\Delta u/\sigma_{\text{load}} = 1$. These conditions are met at the center of the wide loading plates in combination to the rough conditions, as shown by Fig. 11(c). Smooth wide plate and bottom allows for some horizontal displacements affecting the one-dimensional conditions. This results in the ratio $\Delta u/\sigma_{\text{load}}$ reaching values in the order of 0.75, see Fig. 11(a). For plain strain conditions, in which strain increments in one horizontal direction is prohibited and allowed for in the other directions, follows $\Delta p = \sigma_{\text{load}}/2$, resulting in $\Delta u/\sigma_{\text{load}} = 0.5$ (Mandel 1953). These conditions are found at the center of the small loading plates as shown by Figs. 11(c and d).

MPM Analysis

The material point method has been found to be a suitable numerical method for analyzing large deformations in soil penetration problems, such as pile installation and CPT simulation (Kafaji 2013; Galavi et al. 2019; Ceccato et al. 2016; Ghasemi et al. 2018; Martinelli and Pisano 2022; Martinelli and Galavi 2022).

In this paper, the MPM formulation developed by Martinelli and Galavi (2022) is utilized to simulate the centrifuge tests. This choice is motivated by the improved calculation scheme offered by this formulation, which yields accurate contact reaction forces, particularly for contacts between nonporous structures and saturated soils.

The numerical model adopts a dynamic MPM formulation, which employs soil acceleration as the primary unknown variable, and an explicit, conditionally stable time integration method with automatic time step-size adaptation based on the Courant-Friedrichs-Lewy, CFL, criterion. To ensure stable solutions in nonlinear calculations, the critical timestep is multiplied by an additional factor—referred to as the Courant number. This factor remains below 1 and has been set to 0.9 for all simulations presented in this paper.

To simulate plate-soil detachment and sliding, a contact algorithm proposed by Bardenhagen et al. (2000) is used. The background mesh consists of 4-node quadrilateral elements, and a moving mesh technique (Kafaji 2013) is employed to ensure fine discretization around the soil-plate interface and accurate performance of the contact algorithm. Additional computational aspects, such as mass scaling, numerical damping, the mitigation of stress oscillations and volumetric locking, are covered in the original paper of Martinelli and Galavi (2022).

Fig. 12 illustrates the computational mesh for a wide plate, $B = 100$ mm, which consist of 1,726 4-node quadrilateral elements. The initial position of material points across the domain is defined within rectangular clusters. Each cluster contains a predetermined quantity of material points uniformly distributed and specified by the user. This approach ensures that the distribution remains independent of the element type or size. The initial number of material points within the clusters is sufficiently large to fill all elements during penetration, thereby avoiding the creation of unrealistic empty elements.

The MPM simulations simulate the penetration of wide plate. Most of the simulations are performed with smooth contact

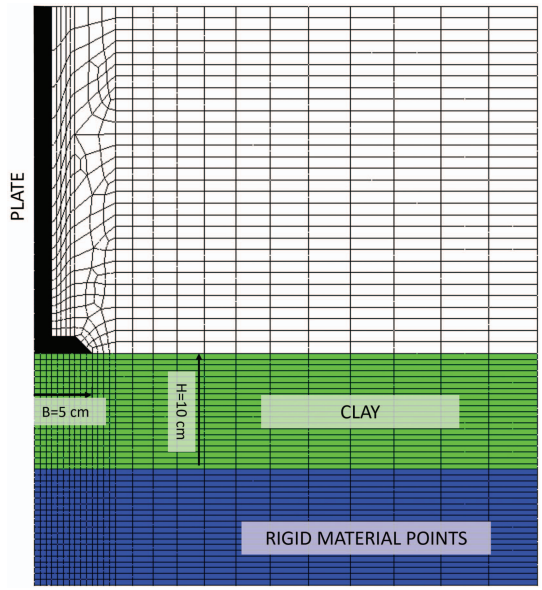

Fig. 12. (Color) Geometry of the MPM model.

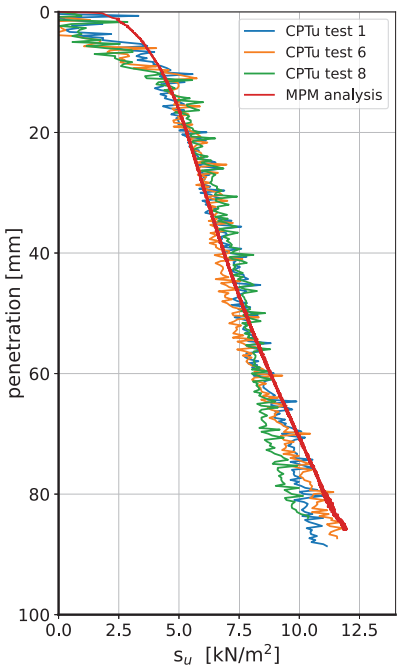

Fig. 13. (Color) Comparison MPM analysis to CPTu data Tests 1, 6, and 8.

Table 5. Model parameters for the modified Cam Clay model

Parameter	Unit	Value
Bulk unit weight, γ_{sat}	kN/m^2	17.2
Porosity, n	—	0.56
Over-consolidation ratio, OCR	—	1.0
Modified compression index, λ^*	—	0.0797
Modified swelling index, κ^*	—	0.0262
Slope of the critical state line (plane strain), M	—	0.538
Poisson's ratio for unl./reload, ν	—	0.3
Coefficient of lateral stress, K_0^{NC}	—	0.73

between the plate and the soil, characterized by absence of adhesion or friction. However, in certain scenarios, a rough contact approach is employed, utilizing very high contact strength properties. This ensures that any failure occurs within the surrounding soil, rather than at the contact nodes. At all boundaries, the displacements are constrained in the perpendicular direction and free in the longitudinal direction.

A set of fixed material points is utilized to impose a fixed boundary condition at the base of the domain. The computational mesh moves together with the plate, while a separate set of material points remains fixed in space to simulate the effect of a rigid container. This approach has been successfully adopted in Talmon et al. (2019) for the simulation of a cutting process of sand underwater.

The modified Cam-Clay constitutive model (a.o. Wood 1990) is used to simulate the compressibility and strength of clay. The model parameters, listed in Table 5, are derived from DSS tests, listed in Table 4. DSS test conditions refer to plane strain conditions as are assumed for the plate loading tests. It is worth noticing that the implementation of the Cam-Clay model used in the numerical simulations gives a Druger-Prager failure state, which is independent of the Lode angle, instead of a Mohr-Coulomb model type of failure. Consequently, the strength parameters employed in plane-strain simulations are selected to match the strength under plane-strain conditions. Conversely, the strength parameters used for triaxial conditions are chosen to match those obtained from triaxial tests.

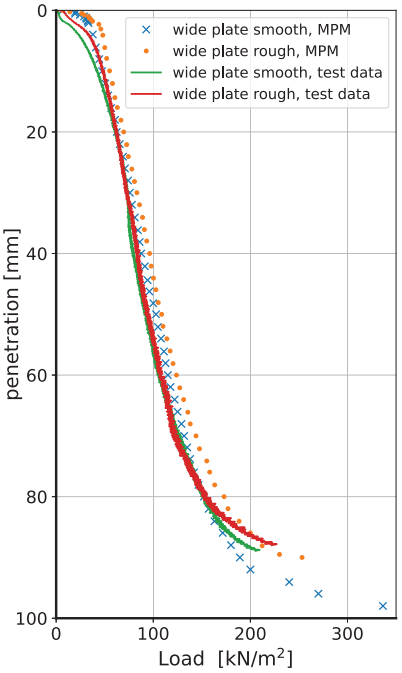

Fig. 14. (Color) Load–displacement curves, comparison MPM analysis to test data Test 1, smooth boundary conditions and Test 8, rough boundary conditions.

Undrained calculations have been performed in which the bulk modulus of water is set to 20 MPa. This value is lower than the true value of 2 GPa to decrease the computational time, while still being large enough to get a high equivalent undrained Poisson's ratio ν_u.

The stress initialization is performed as follows: (1) the stress is kept constant and set to 40 kPa in all soil material points, $K_0^{NC} = 0.73$ and OCR $= 1$; (2) the gravitational acceleration is then increased to 100 g, and the excess pore pressures are

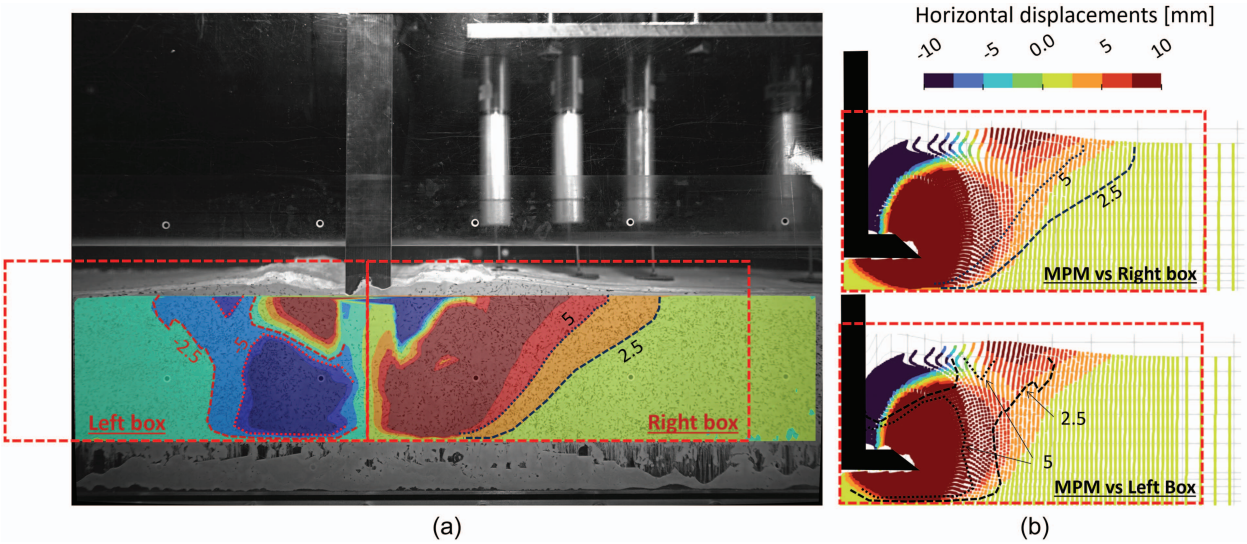

Fig. 15. (Color) Horizontal displacement field for wide plate and smooth boundaries at a penetration depth of 82 mm: (a) PIV analysis of test data; and (b) numerical analysis. The same scale is used in both figures.

calculated using an undrained simulation; and (3) the final profile of OCR is obtained through a 2-phase coupled analysis, during which the excess pore pressures are completely dissipated. In the last step, in order to reduce computational costs, a high value of hydraulic conductivity is adopted for the clay.

To verify the MPM schematization and parameter assessment, the CPTu data is back calculated. In this case, the simulations are performed with a 2-phase coupled approach, as described in Martinelli and Galavi (2022), to ensure correct contact forces between the cone and the soil. The contact friction angle is set to 11 degrees and the soil permeability is set to 1×10^{-7} m/s. This value is larger than true soil permeability, but it is low enough to ensure undrained response during penetration. The slope of the critical state line, M is set to 0.6935.

Fig. 13 shows that MPM simulation of the CPTu data is in close agreement to the centrifuge data. Therefore, it is concluded that the MPM schematization, the applied material model and selected parameters provide a reliable description of the clay behavior.

Fig. 14 shows a comparison between the measured and simulated load - displacement curves. The simulations for smooth boundary conditions are in good agreement to the measurement data. For rough boundary conditions the numerical analysis seems to slightly overpredict the plate resistance.

Figs. 15 and 16 show a comparison of the horizontal and vertical displacement fields, found from the test data by PIV analysis and found by the numerical analysis. The small gap between the loading plate and the front wall might have an impact on the displacement observed in the tests. Especially the nearby displacements at the transparent wall might be different from displacements found in a cross section including the plate. Therefore, the comparison is focused on the far field displacements. Figs. 15 and 16 show the 5 mm and the 2.5 mm contour for vertical displacements and the 3.3 mm and 1.1 mm contour for the horizontal displacements found

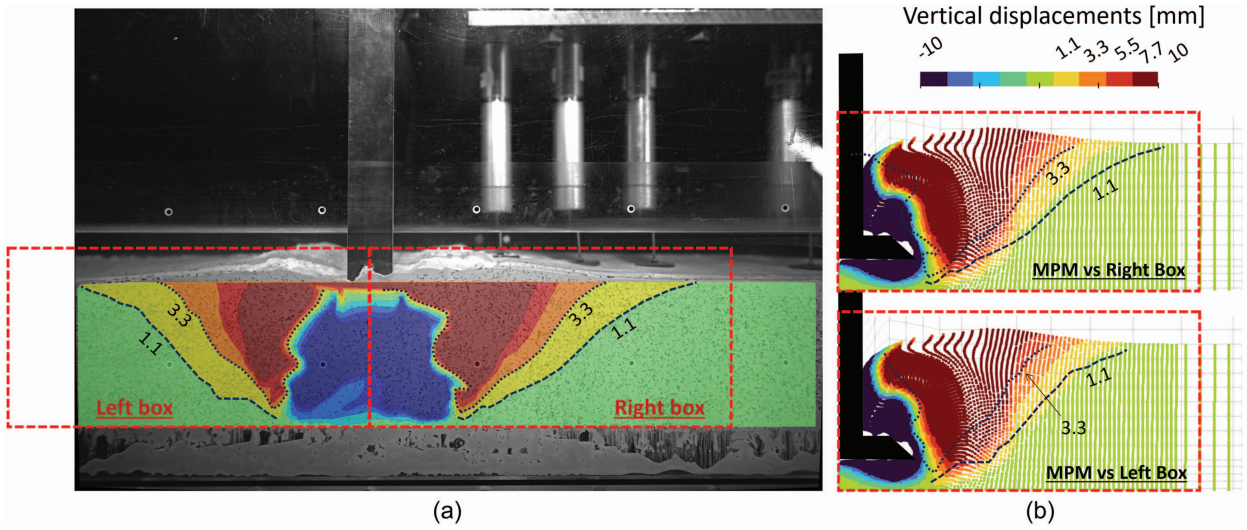

Fig. 16. (Color) Vertical displacement field for wide plate and smooth boundaries at a penetration depth of 82 mm: (a) PIV analysis of test data; and (b) numerical analysis. The same scale is used in both figures.

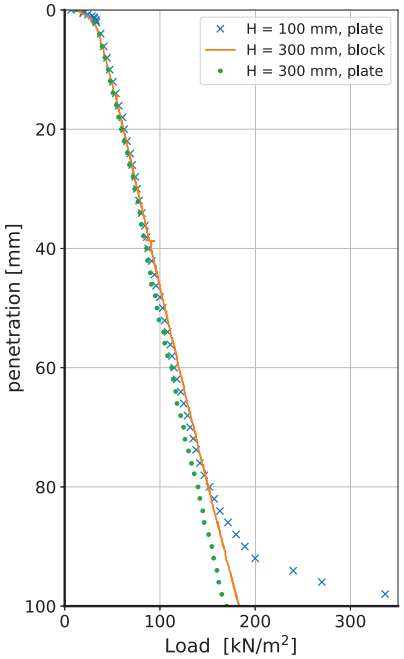

Fig. 17. (Color) Influence layer thickness and shaft width, H = initial layer thickness.

in the PIV analysis. To facilitate the comparison these contours are plotted in the MPM results. The PIV analysis shows that the displacements fields in the test are not completely symmetrical. A good agreement is found between the far field displacements found in PIV analysis and MPM analysis.

Discussion

Section "Theoretical Background" introduces two effects that influence the plate resistance. The first effect is the finite layer effect, which causes an increase in resistance for reducing thickness. The second effect is the gap, that is formed above the plate during penetration and the corresponding backflow. This effect results in a reduction of the resistance as soon as the backflow develops.

To study the individual effects, two additional MPM analyses have been conducted. The first analysis contains a 100 mm penetration of the wide plate in a 300 mm thick clay layer. Fig. 17 compares the outcome to the original analysis. The comparison clearly shows the increase in resistance, starting at a penetration depth of 60 mm, when penetration depth reaches the initial layer thickness.

The second analysis contains the penetration of a block with the same width as the wide plate, $B = 100$ mm. The uniform width of the block prevents cavity development, and no backflow occurs during penetration. Fig. 17 shows the comparison of the 100 mm penetration of a block and plate both in a 300 mm thick clay layer. The figure clearly shows the reduced resistance for the plate, including the cavity. This reduction can be explained as follows; for the block geometry, clay below the plate cannot flow around the tip of the plate and lateral stress will be build up against the shaft. When the shaft is smaller than the plate, the clay can flow around the tip, filling the open space above the plate without the lateral resistance from the shaft.

As mentioned in the section "Centrifuge Test Results," the impact of the bottom and plate roughness on the stress–strain curves, Fig. 6, seems remarkably small. A further analysis of the measurement data shows a difference in pore pressure response for the different boundary conditions. Fig. 18 shows the pore pressure

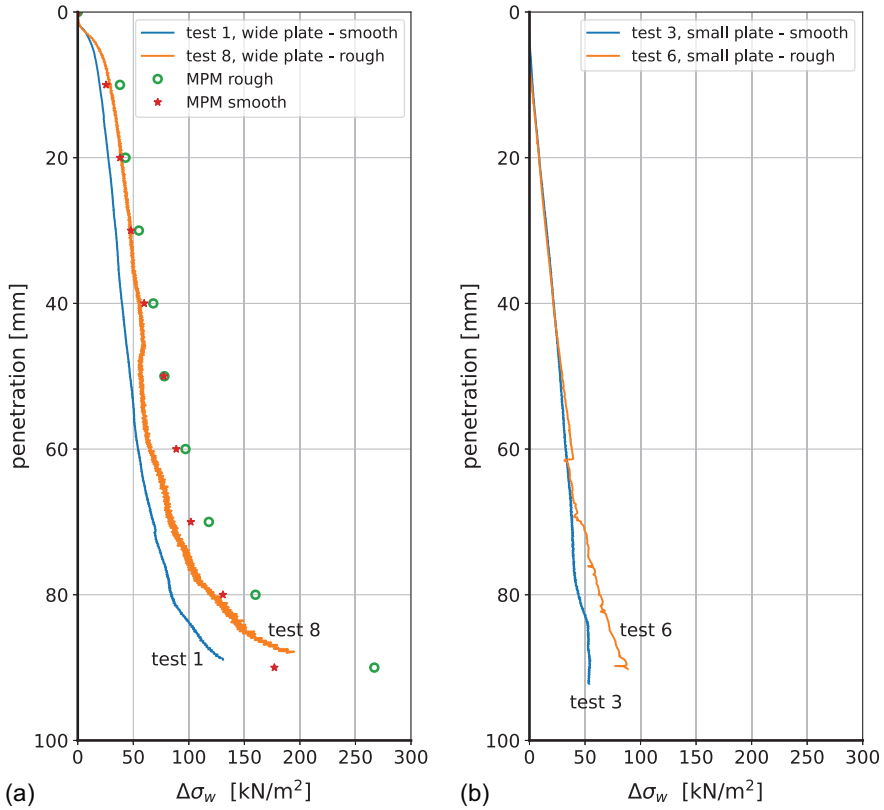

Fig. 18. (Color) Pore pressure increments at the bottom of the clay layer: (a) measurements of P10 and MPM simulations for wide plate; and (b) measurements of P11 for small plate. For positions of P10 and P11 see Fig. 2.

response measured below the approaching plate at the bottom of the clay layer. For the wide plate, the pore pressure increment for rough boundary conditions is larger than found for smooth boundary conditions. For the small plate the pore pressure increment is equal for smooth and rough boundary conditions, until a penetration depth of 45 mm. For larger penetration depths, rough boundary conditions, result in larger pore pressure increments. Fig. 18 shows that the numerical analysis overpredicts the pore pressure response but supports the trend. The rough boundary conditions result in larger pore pressure response than found for the smooth boundary conditions.

The differences in pore pressure development can explain the limited influence of the bottom roughness on the measured load in Fig. 6. Following Eq. (3), a pore pressure increment causes a reduction in s_u. The larger pore pressure increment for the rough boundary conditions results in a lower activated s_u than found for the smooth boundary conditions. Consequently, the differences in resistance due to differences in bottom roughness is counterbalanced by a difference in pore pressure generation and corresponding undrained shear strength.

Conclusions

A series of plate loading tests have been conducted successfully and data is available through Zwanenburg et al. (2023b). The test results are used for validation of numerical tools with a focus on geometrical nonlinearities. The tests comprise two sources of geometrical nonlinearity. The first follows from the reducing clay layer thickness during penetration of the plate. The second follows from the backflow around the tip of the plate.

A good agreement is found between the measurement data and numerical analyses for the load–displacement curves. Both effects of geometrical non-linearity are identified in the numerical analysis. The finite layer effect is found for the wide plate at a penetration depth of 70 mm, $B/H = 3.33$. For the small plate, the effect is found for a penetration of approximately 85 mm, $B/H = 1.33$.

The gap created above the plate during penetration and the corresponding backflow has a clear reducing impact on the measured resistance.

While the analytical solutions are only available for the load - displacement curves, the centrifuge data allows to validate the numerical analysis on additional aspects. As such a good agreement is found for the horizontal and vertical displacement fields. The numerical analysis slightly overpredicts the pore pressure development below the plate.

The differences between tests with smooth and rough boundary conditions are remarkably small, which is explained by the difference in pore pressure development. For the rough conditions a larger pore pressure response is found than found for smooth conditions. The larger pore pressure response has a reducing effect on the shear strength mobilization and consequently the total resistance.

Data Availability Statement

All experimental data generated in this study is available online at Zwanenburg et al. (2023b): https://doi.org/10.5281/zenodo.8066899.

Acknowledgments

The authors would like to thank Deltares for financing this study. Also, the authors would like to thank the Deltares centrifuge crew for preparing and running the centrifuge tests. All MPM simulations were performed using a version of Anura3D developed in-house by Deltares.

Notation

The following symbols are used in this paper:

A = superficial area of the plate;
A_c = projected cone area;
a = cone area ratio, here $a = 0.54$;
B = width of the plate;
c' = soil cohesion;
D_{cone} = cone diameter;
D_{sleeve} = sleeve diameter of CPTu cone;
d = shaft width, see Fig. 1(c);
e = void ratio;
F_c = measured force;
H = remaining height of the clay below the plate;
h_{sleeve} = length sleeve of CPTu cone;
h_{tip} = tip height of CPTu cone;
K_0 = ratio of horizontal to vertical effective stress;
L_{cptu} = distance between the CPTu and nearest side wall;
M = tangent of the critical state line (plane strain);
m = exponent, parameter of SHANSEP formulation;
N_c, N_{cd} = bearing capacity factor, bearing capacity factor for the backflow mechanism, see Eq. (2);
N_{kt} = bearing capacity factor cone, see Eq. (5), here $N_{kt} = 14$;
q_{u} = undrained bearing strength;
q_c, q_t, q_{net} = cone resistance, cone resistance corrected for pore pressure, cone resistance corrected for pore pressure and overburden pressure;
S = undrained shear strength ratio at normally consolidated conditions;
s_{u} = undrained shear strength;
s_x, s_y = total horizontal displacement, total vertical displacement;
u, u_0 = pore pressure, pore pressure in steady state conditions;
u_2 = pore pressure measured just behind the cone;
V = volume embedded plate;
w = water content;
w_{L} = liquid limit;
Δp = isotropic total stress increment;
γ' = effective weight of the soil;
γ_{sat} = bulk unit weight;
φ'_{tc} = angle of internal friction in triaxial compression;
θ = apex angle;
κ^* = modified swelling index;
λ^* = modified compression index;
ν = Poisson's ratio for unl./reload;
σ_{load} = applied loading stress;
σ_{v}, σ'_{v} = overburden pressure, vertical effective stress respectively; and
σ'_{vc} = pre-consolidation stress.

References

ASTM. 2012. *Standard test method for one-dimensional consolidation properties of saturated cohesive soils using controlled strain loading*. ASTM D4186-06. West Conshohocken, PA: ASTM.

ASTM. 2017. *Standard test method for consolidated undrained direct simple shear testing of fine grains*. ASTM D6528-07. West Conshohocken, PA: ASTM.

Bardenhagen, S., J. Brackbill, and D. Sulsky. 2000. "The material point method for granular materials." *Comput. Methods Appl. Mech. Eng.* 187 (3–4): 529–541. https://doi.org/10.1016/S0045-7825(99)00338-2.

Brinch Hansen, J. 1970. *A revised and extended formula for bearing capacity, a reprint of lecture in Japan (1968). Bulletin No. 28*. Lyngby, Denmark: Danish Geotechnical Institute.

Buisman, A. S. 1940. *Grondmechanica [Soil mechanics]*. [In Dutch.] Rotterdam: Balkema.

Ceccato, F., L. Beuth, P. A. Vermeer, and P. Simonini. 2016. "Two-phase material point method applied to the study of cone penetration." *Comput. Geotech.* 80 (2016): 440–452. https://doi.org/10.1016/j.compgeo.2016.03.003.

Das, B. M. 2007. *Shallow foundations, bearing capacity and settlement*. 3rd ed. Boca Raton, FL: CRC Press.

De Josselin De Jong, G. 1963. "Consolidatie in drie dimensies [Consolidation in three dimensions]." [In Dutch.] *LGM Mededelingen* deel VII (3): 57–73.

Den Haan, E. J., and S. Kamao. 2003. "Obtaining isotach parameters from a CRS K0 oedometer." *Soils Found.* 43 (4): 203–214. https://doi.org/10.3208/sandf.43.4_203.

Dyvik, R., T. Berre, S. Lacasse, and B. Raadim. 1987. "Comparison of truly undrained and constant volume direct simple shear tests." *Géotechnique* 37 (1): 3–10. https://doi.org/10.1680/geot.1987.37.1.3.

Galavi, V., M. Martinelli, A. Elkadi, P. Ghasemi, and R. Thijssen. 2019. "Numerical simulation of impact driven off-shore monopiles using the material point method." In *Proc., 17th ECSMGE*, edited by H. Sigursteinsson, S. Erlingsson, and B. Bessason, 1–6. Reykjavik, Iceland: Icelandic Geotechnical Society.

Ghasemi, P., M. Calvello, M. Martinelli, V. Galavi, and S. Cuomo. 2018. "MPM simulation of CPT and model calibration by inverse analysis." In *Proc., 4th Int. Symp. on Cone Penetration Testing (CPT'18)*, edited by M. A. Hicks, F. Pisanò, and J. Peuchen, 295. Leiden, Netherlands: CRC Press.

Hossain, M. S., M. F. Randolph, and Y. Hu. 2004. "Bearing behaviour of spudcan foundation on uniform clay during deep penetration." In *Proc., 23rd Int. Conf. on Offshore Mechanics and Arctic Engineering, Vancouver, Canada*. New York: ASME.

Hossain, M. S., M. F. Randolph, Y. Hu, U. Curtin, and D. J. White. 2006. "Cavity Stability and Bearing Capacity of Spudcan Foundations on Clay." In *Proc., Offshore Technology Conf.* Houston: Offshore Technology Conference.

Kafaji, I. K. 2013. "Formulation of a dynamic material point method (MPM) for geomechanical problems." Ph.D. thesis, Fakultät für Bau – und Umweltingenieurwissenschaften, Institut für Geotechnik, Univ. of Stuttgart.

Ladd, C. C., and R. Foot. 1974. "New design procedure for stability of soft clays." *J. Geotech. Eng. Div.* 100 (7): 763–786. https://doi.org/10.1061/AJGEB6.0000066.

Leroueil, S., J. P. Magnan, and F. Tavenas. 1990. *Embankments on soft clays*. Chichester, UK: Ellis Horwood.

Mandel, J. 1953 "Consolidation des Sols (étude mathématique). [Consolidation of soils (a mathematical study)]." [In French] *Géotechnique* 3 (7): 287–299. https://doi.org/10.1680/geot.1953.3.7.287.

Martinelli, M., and V. Galavi. 2022. "An explicit coupled MPM formulation to simulate penetration problems in soils using quadrilateral elements." *Comput. Geotech.* 145 (2022): 104697. https://doi.org/10.1016/j.compgeo.2022.104697.

Martinelli, M., and F. Pisano. 2022. "Relating cone penetration resistance to sand state using the material point method." *Géotech. Lett.* 12 (2): 1–8. https://doi.org/10.1680/jgele.21.00145.

Meyerhof, G. G. 1951. "The ultimate bearing capacity of foundations." *Géotechnique* 2 (4): 301. https://doi.org/10.1680/geot.1951.2.4.301.

Meyerhof, G. G. 1963. "Some recent research on the bearing capacity of foundations." *Can. Geotech. J.* 1 (1): 16. https://doi.org/10.1139/t63-003.

NNI (Nederlands Normalisatie Instituut). 2018. *Geotechnical investigation and testing—Laboratory testing of soil—Part 12: Determination of liquid and plastic limits*. NEN-EN-ISO 17892-12/CSN EN ISO 17892-12. Delft, Netherlands: NNI.

Prandtl, L. 1920. "Über die Härte plastischer Körper. [On the hardness of plastic bodies]." [In German.] In *Nachrichten der Gesellschaft der Wissenschaften zu Göttingen, Mathematisch-physikalischen Klasse*, 74–85. Göttingen, Germany: Gesellschaft der Wissenschaften.

Robertson, P. K., and K. L. Cabal. 2015. *Guide to cone penetration testing for geotechnical engineering*. 6th ed. Signal Hill, CA: Gregg Drilling & Testing Inc.

Stanier, S., J. Blader, W. A. Take, and D. J. White. 2015. "Improved image-based deformation measurement for geotechnical applications." *Can. Geotech. J.* 53 (5): 727–739. https://doi.org/10.1139/cgj-2015-0253.

Talmon, A. M., M. Martinelli, and H. J. Luger. 2019. "Numerical simulation of cutting tests on layered sand and clay." In *Proc., 22nd World Dredging Congress (WODCON 2019)*, 462–477. Delft, Netherlands: Central Dredging Association.

Ullah, S. N., and X. Hu. 2017. "Large deformation modelling of soil squeezing and its application to spudcan in clay with interbedded sand." *Int. J. Offshore Polar Eng.* 27 (4): 383–389. https://doi.org/10.17736/ijope.2017.tm82.

Ullah, S. N., Y. Hu, S. A. Stanier, and D. White. 2016. "Lateral boundary effects in centrifuge foundation tests." *Int. J. Phys. Modell. Geomech.* 17 (3): 144–160. https://doi.org/10.1680/jphmg.15.00034.

Van Baars, S. 2018. *100 years of Prandtl's wedge*. Amsterdam: IOS Press.

Wood, D. M. 1990. *Soil behaviour and critical state soil mechanics*. Cambridge, UK: Cambridge University Press.

Zwaan, R., J. Terwindt, D. de Lange, and A. Bezuijen. 2020. "A new geotechnical centrifuge at Deltares, Delft, the Netherlands." In *Proc., 4th European Conf. on Physical Modelling in Geotechnics (Laue & Bansal eds) Lulea, Sweden*. Lulea, Sweden: Lulea Univ. of Technology.

Zwanenburg, C., B. Wittekoek, M. Martinelli, and E. Alderlieste. 2023a. "The effect of finite layer thickness: A validation of MPM analysis by centrifuge testing." In *Proc., 10th European Conf. on Numerical Methods in Geotechnical Engineering, NUMGE*, edited by L. Zdravković, S. Konte, D. M. G. Taborda, and A. Tsiampousi. London: International Society for Soil Mechanics and Geotechnical Engineering.

Zwanenburg, C., B. Wittekoek, M. Martinelli, E. Alderlieste, and R. Zwaan. 2023b. "Calibration chamber for numerical tools." Zenodo. Accessed June 27, 2024. https://doi.org/10.5281/zenodo.8066899.